Physics of the Earth and Planetary Interiors 297 (2019) 106320

Contents lists available at ScienceDirect

Physics of the Earth and Planetary Interiors

journal homepage: www.elsevier.com/locate/pepi

Nonlinear dynamics of crustal blocks and faults and earthquake occurrences in the Transcaucasian region

Inessa Vorobieva[a], Alik Ismail-Zadeh[b,*], Alexander Gorshkov[a]

[a] Russian Academy of Sciences, Institute of Earthquake Prediction Theory and Mathematical Geophysics, Moscow, Russia
[b] Karlsruhe Institute of Technology, Institute of Applied Geosciences, Karlsruhe, Germany

ARTICLE INFO

Keywords:
Caucasus
Crustal block
Dynamics
Earthquake
Fault slip
Numerical modeling
Transcaucasia

ABSTRACT

The Caucasus is a part of ongoing collision of the Arabian and Eurasian plates, where moderate to strong earthquakes caused significant losses of lives and livelihood in the past. To better understand seismic hazard in the region, we develop a model of block-and-fault dynamics for Transcaucasia, the largest part of the Caucasus to the south of the Greater Caucasus Mountains, to simulate regional earthquakes. The model structure is developed by employing the results of the morphostructural analysis to delineate crustal blocks and the geodetic observations on crustal movements in the region. The model incorporates a nonlinear rate-dependent slip of the faults separating the blocks. A set of numerical experiments has been performed to address the following questions: (i) where strong earthquakes occur and what their reoccurrence time is; (ii) how rigid crustal blocks react to the Arabian plate push and to movements of the ductile part of the crust in Transcaucasia; and (iii) whether the fault slip rates and the block displacements in the model correlate with observed GPS-velocities. The model results confirm that the contemporary crustal dynamics and seismicity pattern in Transcaucasia are determined by the north-northeastern motion of the Arabian plate relative to Eurasia and by the movement of the ductile crust underlying the rigid crustal blocks. Variations in the rheological properties of the fault zones and/or of the ductile crust influence the pattern of seismicity. The number and maximum magnitude of synthetic earthquakes change with the variations in the movements of the crustal blocks and in the rheological properties of the lower crust and the fault zones. The model results can be used in comprehensive seismic hazard assessment of the Caucasus region based on instrumentally observed, historical and synthetic seismicity.

1. Introduction

The Caucasus region is a part of ongoing collision of the Arabian and Eurasian plates, which is often compared to the collision zone between India and Eurasia during its early stages of evolution (e.g., Şengör and Kidd, 1979). For > 100 Ma the convergence resulted in closure of the Neo-Tethys Ocean and subduction of its lithosphere beneath Eurasia (e.g., Dewey et al., 1973; Khain, 1975). Seismological, geophysical, geodetic, and geological studies refined the plate tectonic characterization of the region, including partitioning of crustal deformation in the eastern Turkey and Caucasus continental collision zone (Jackson, 1992; Allen et al., 2004; Copley and Jackson, 2006), and the beginning of subduction of the South Caspian oceanic basin beneath the North Caspian continental lithosphere along the Central Caspian Seismic Zone (e.g., Jackson et al., 2002). The Greater Caucasus is thought to have formed by tectonic inversion of a former back-arc basin developed on continental crust, that opened during the early Mesozoic above the north-dipping subduction of the Neotethys (e.g., Adamia et al., 1981; Zonenshain and Le Pichon, 1986; Mosar et al., 2010). The eastern Black Sea and southern Caspian Sea are remnants of oceanic basin developed in the Cretaceous and Jurassic times, respectively. The continued convergence generated a compressive stress field reactivating the deformation and uplift of the Greater Caucasus in the Pliocene (e.g., Saintot and Angelier, 2002).

Caucasus is an earthquake-prone region (Fig. 1), where moderate to strong (often devastating) earthquakes caused significant losses of lives and/or livelihood and damaged infrastructure. The 1139 Ganja (Azerbaijan) M7.3 earthquake resulted in about 200,000–300,000 death toll (Ulomov and Medvedeva, 2014). Due to this earthquake a part of the Kapaz Mount was collapsed and blocked the Kürakçay River creating the Lake Göygöl. Significant event occurred in 1275 (M6.7 ± 0.7 earthquake) in Mtskheta (Georgia) causing huge landslides, which buried many settlements (Kondorskaya and Shebalin, 1977). Several devastating earthquakes hit the city of Shamakha (Azerbaijan) since at

* Corresponding author at: KIT-AGW, Adenauerring 20b, Karlsruhe 76131, Germany.
E-mail address: alik.ismail-zadeh@kit.edu (A. Ismail-Zadeh).

https://doi.org/10.1016/j.pepi.2019.106320
Received 30 April 2019; Received in revised form 1 July 2019; Accepted 24 September 2019
Available online 23 October 2019

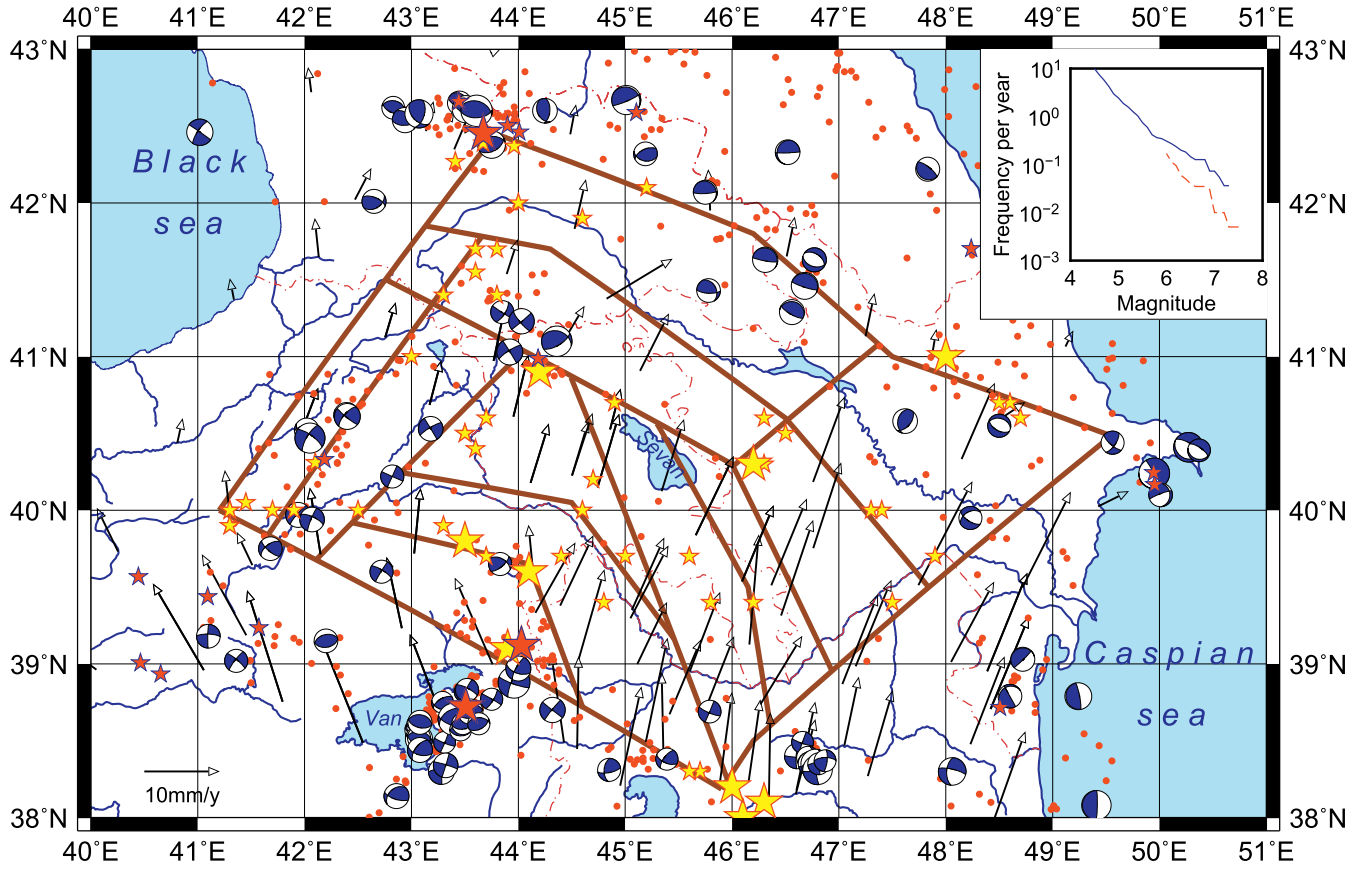

Fig. 1. Map of the Caucasus region with earthquakes. Instrumentally recorded earthquakes are marked by red dots (magnitude M4.5+), by small red stars (M6+), and big red starts (M7+) (ANSS catalog for the period of 1974–2017; https://earthquake.usgs.gov/monitoring/anss/). Historical strong earthquakes as well as instrumentally recorded seismicity for the period from 1000 to 1973 are marked by small yellow starts (M6+) and big yellow starts (M7+) (Ulomov and Medvedeva, 2014). Black arrows: GPS velocities (Vernant and Chery, 2006, Djamour et al., 2011, Karakhanyan et al., 2013). Black-white balls are the earthquakes mechanisms obtained from the Global Centroid-Moment-Tensor solution (CMT; https://www.globalcmt.org/). Brown lines separate the model blocks (see Fig. 3). Insert (the upper right panel): Frequency-magnitude relationship for earthquakes in the Caucasus region. The blue curve represents the data from the ANSS earthquake catalog; and the red curve represents the data from Ulomov and Medvedeva (2014) since 1800, M ≥ 6.0. (For interpretation of the references to color in this figure legend, the reader is referred to the web version of this article.)

least the middle 17th century. The 1667 strong M7.8 earthquake (perhaps the strongest historically-recorded event in Caucasus) killed about 80,000 inhabitants, and its 1669 powerful M6.0 ± 0.7 aftershock other 6000 to 7000 people. Less powerful M6.5 earthquake in 1859 was so destructive that the Governor's seat and governmental institutions were transferred from Shamakha to Baku. In 1872, another M6.0 shock occurred, and it triggered emigration of people to Baku. The last devastating M6.9 ± 0.2 earthquake in Shamakha occurred on 13 February 1902; about 2000 people – about 10% of the total population of the city – were perished; 4000 houses were destroyed; a mud volcano near Shamakha started to erupt (Kondorskaya and Shebalin, 1977; Ulomov and Medvedeva, 2014).

Historical data are important for understanding of earthquake occurrences, but the data have shortcoming, because the information on historical earthquakes is limited and insufficient to analyze a particular event in some detail. For example, isoseismals are usually incomplete, and the number of observed localities is limited. This results in an inaccuracy of assessment of earthquakes parameters, such as depth and intensity damping. Instrumental observations of earthquakes in the Caucasus began by the installation of a horizontal Rebeur-Ehlert pendulum seismograph in the Tbilisi seismic station in 1899 (Tskhakaia, 1950); after the 1902 Shamakha earthquake several seismographs and pendulum were installed in the region (e.g., Veber, 1904). In early 1970th broadband seismic recording instruments were introduced, and the number of seismic stations in the Caucasus increased to thirty (Panahi, 2006). Seismic network resolution in the Caucasus was significantly improved for the last decades. National networks deployed new seismic stations and established good collaboration in exchanging online waveform data.

Eight strong earthquakes of magnitude 6.8 and greater occurred in the region from 1900 to present (Table 1) with devastating events such as the 1988 Mw6.9 Spitak (Armenia) and the 1991 Mw7.0 Racha (Georgia) earthquakes. The Spitak earthquake caused the immense human casualties (about 25,000 people were killed), the city of Spitak and Leninakan were destroyed to 90% and 50%, respectively (Cisternas et al., 1989). The Racha earthquake resulted, fortunately, in a smaller (compared to the Spitak earthquake case) loss of human lives but still caused significant destruction within densely populated areas (Adamia et al., 2017).

The annual frequency to magnitude relationship for the regional earthquakes (Fig. 1, insert) is based on the instrumentally recorded and historical data. The frequency-magnitude curve for strong earthquakes (M ≥ 6.0) including historical events from 1800 (dashed curve) fits well the slope of that from instrumentally-recorded events of magnitude M < 6, for the last several decades (solid curve). This assumes that the historical catalog is complete for M ≥ 6.0 during last two centuries, and the deviation from the linearity of the solid curve is associated with the short period of instrumental observations (1973–2017). The downward deviation from the solid curve could also be explained as the deficiency of strong earthquakes in the historical catalog, which does not record

Table 1
Strong (M6.8+) earthquakes in the Caucasus and the surrounding region (sources: Ulomov and Medvedeva, 2014; and ANSS for the period since 1973).

Place	Date	Epicenter (lat. N, lon. E)	Focal depth (km)	Magnitude
Iran	1042	38.1, 46.3	16	7.6
Ganja	1139	40.3, 46.2	16	7.3
Turkey	1319	39.8, 43.5	30	7.4
Iran	1550	38.0, 46.1	14	7.3
Shamakha (Azerbaijan)	14.01.1668	41.0, 48.0	40	7.8
Chaldiran	14.06.1696	39.1, 43.9	10	7.0
Tabriz	08.01.1780	38.2, 46.0	18	7.7
Turkey	02.07.1840	39.6, 44.1	22	7.2
Shamakha (Azerbaijan)	13.02.1902	40.7, 48.6	18	6.9
Erzurum (Turkey)	13.09.1924	40.0, 42.0	10	6.9
Turkey-Iran border	24.11.1976	39.121, 44.029	36	7.5
Narmar (Turkey)	30.10.1983	40.330, 42.187	15	6.8
Spitak (Armenia)	07.12.1988	40.987, 44.185	5	6.9
Racha (Georgia)	29.04.1991	42.453, 43.673	17.2	7.0
Caspian	25.11.2000	40.245, 49.946	50	6.8
Van (Turkey)	23.10.2011	38.721, 43.508	18	7.1

the events that could occur in non-populated areas of the region.

The main motivation of our study was to understand better occurrences of strong earthquakes in the Caucasian region and their average recurrence time. By employing the results of morphostructural analysis delineating major crustal blocks, regional active faults, and earthquake simulations (numerical experiments), we have studied dynamics of the crustal blocks and the faults separating them. The earthquake simulator initially proposed by Gabrielov et al. (1990) has been further developed to include a fault slip depending on a nonlinear inelastic displacement rate. This simulator has been applied to generate synthetic seismicity in Transcaucasia, the largest part of the Caucasus to the south of the Greater Caucasus Mountains. Earthquake simulations help in studies of seismic hazard assessment using instrumentally recorded, historical and simulated earthquakes (e.g., Sokolov and Ismail-Zadeh, 2015, 2016). Therefore, the principal goal of this research is to identify the areas prone to strong earthquakes in the Transcaucasian region and estimate their average recurrence times.

Following the earlier study of the dynamics of the Tibet-Himalayan lithosphere and earthquake occurrences (Ismail-Zadeh et al., 2007) and the similarity of the continent-continent collision in the Caucasus and Tibet regions (Şengör and Kidd, 1979), we study a block-and-fault dynamics model (BAFD model) for Transcaucasia in order to answer the following questions: (i) how rigid crustal blocks react to the Arabian plate push and to movements of the ductile part of the crust in Transcaucasia; (ii) where strong seismicity occur in the system of major regional faults; (iii) whether the focal mechanisms of model seismic events are comparable with the mechanisms of observed earthquakes; and (iv) whether the fault slip rates and the block displacements in the model correlate with observed GPS-velocities. In sect. 2, we present the basic principles and mathematical statement of the BAFD model emphasizing the nonlinear rheological behavior of the blocks-and-faults interaction. The block model geometry of the Transcaucasian region and model parameters used are discussed in sect. 3. We present the results of our numerical experiments in sect. 4, and discuss them in sect. 5 before arriving to concluding remarks (sect. 6).

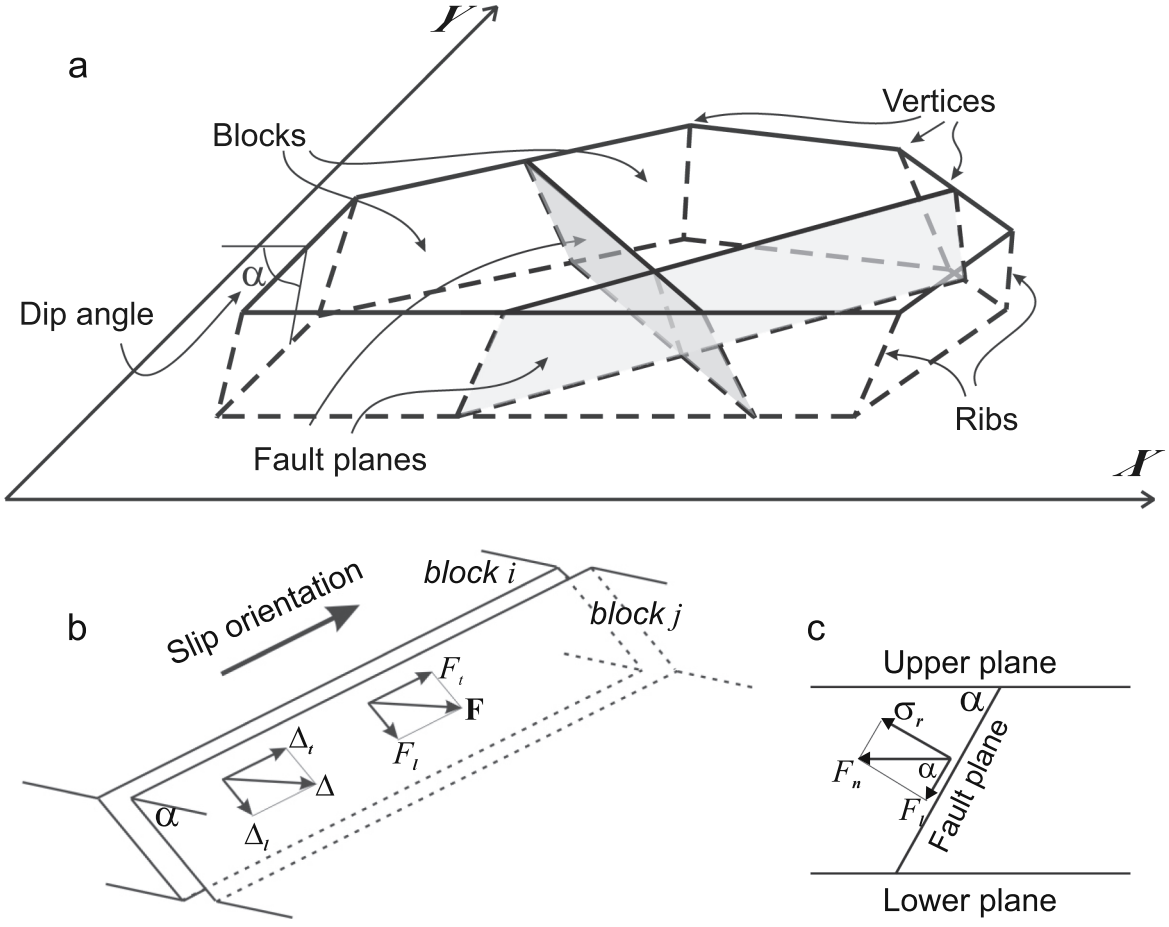

Fig. 2. Structure of a BAFD model. (a) Model geometry. (b) Relative displacements of blocks and the forces per unit area in the fault plane. A vertical section of a block-and-fault structure orthogonal to a fault presenting (c) the forces per unit area. Modified after Ismail-Zadeh et al. (2018).

2. BAFD model

2.1. Basic principles and governing equations

A block-and-fault dynamics (BAFD) model is used to analyze how the basic features of seismicity depend on the crust (lithosphere) structure and dynamics. The basic principles of the model have been developed by Gabrielov et al. (1990) and further developed by Soloviev and Ismail-Zadeh (2003). The BAFD model considers a seismic region as a structure of perfectly rigid (upper crustal or lithospheric) blocks divided by infinitely thin fault planes. The model can be used in studies of the interaction between the rigid upper crust and the ductile lower crust as well as between the lithosphere itself and the asthenosphere. The block-and-fault structure considered in the model is a bounded and simply connected part of a layer of thickness H limited by two horizontal planes (Fig. 2a). The lateral boundaries of the structure and its subdivision into blocks are formed by portions of planes intersecting the layer; we refer to these planes as fault planes. The intersection lines of the fault planes with the upper plane are referred to as faults. The fault planes may have arbitrary dip angles, which are specified in the model on the basis of the knowledge of the deep structure of the region under study. A common point of two faults is referred to as a vertex. The vertices in the upper and the lower planes are connected by a rib of the intersection line of the relevant fault planes (Fig. 2a). The part of a fault plane between two ribs corresponding to successive vertices on the fault is referred to as a fault segment. The upper and the lower surfaces of the blocks are polygons. The common part of a block with the lower plane is referred to as a block bottom. The block-and-fault structure is bordered by the infinite confining medium. The motion of the confining medium is defined in areas bounded by two ribs of the structure boundary (refer to each area as a boundary block). The blocks interact between themselves and with the underlying medium (lower crust or asthenosphere) and move in response to prescribed motion of the boundary blocks and of the underlying medium. Dimensionless time is used in the model. At each time step the translation vectors and the angles of rotation of the blocks are determined in such a way that the structure is in a quasi-static equilibrium.

Because the blocks are perfectly rigid, deformation is localized in the fault zones. Relative block displacements take place along the fault planes, and elastic forces arise in the planes as a response to the displacements. The elastic force per unit area $\mathbf{F} = (F_t, F_l)$ at point (X, Y) of the fault plane, separating two blocks i and j (Fig. 2b), is calculated as:

$$F_t = K(\Delta_t - \delta_t), \quad F_l = K(\Delta_l - \delta_l), \tag{1}$$

where $\delta = (\delta_t, \delta_l)$ is the inelastic displacement at the considered point of the fault plane, parallel(δ_t) and perpendicular (δ_l) to the fault. The inelastic displacement at point (X, Y) depends on time as.

$$\frac{d\delta_t}{dt} = WF_t, \frac{d\delta_l}{dt} = WF_l. \tag{2}$$

In Eqs. (1) and (2), $K = \mu/a$ is the elastic parameter (measured in 10^7 Pa m^{-1}), and $W = a/\eta$ is the inelastic parameter (measured in 10^{-7} m Pa^{-1} yr^{-1}), where μ and η are the shear modulus and the effective viscosity of the fault zone, and a is the characteristic length ($a = 3$ km is assumed in the model). In the classical BAFD model, the effective viscosity (and hence W) of the fault zone is constant, and this leads to the Maxwell rheological law for the stress-strain relation (e.g., Soloviev and Ismail-Zadeh, 2003).

In this analysis, we introduce a nonlinear rate-dependent slip at the faults, that is, the rheological parameter W (or the effective viscosity) depends on the inelastic displacement rate $\dot{\delta}$ expressed in the form:

$$W = W_0 \ |\dot{\delta}|^{(n-1)/n}, \ |\dot{\delta}| = \sqrt{\left(\frac{d\delta_t}{dt}\right)^2 + \left(\frac{d\delta_l}{dt}\right)^2}, \tag{3}$$

where W_0 corresponds to the linear viscosity, and $\dot{\delta} \approx (\delta^{(t)} - \delta^{(t-1)})/\Delta t$ is determined as the ratio between the difference of the inelastic displacement at the current time $\delta^{(t)}$ and the previous time $\delta^{(t-1)}$ and time step Δt. At $n = 1$, we get a linear viscous slip, and at $n \to \infty$, a perfectly plastic slip (e.g., Ismail-Zadeh and Tackley, 2010). We used $n = 2$ in all (except one) numerical experiments presented in this paper; in this case, the dimensional number W_0 equals to 3.16×10^{-4} m$^{1/2}$ Pa^{-1} yr$^{-1/2}$.

In addition to the elastic force, there is a reaction force normal to the fault plane; the work of this force is zero, because all relative movements are tangent to the fault plane. The horizontal component F_n of the elastic force per unit area, which is normal to the considered fault (the intersection between the fault plane and the upper plane of the block), can be expressed as $F_n = F_l/\cos\alpha$. Hence, the force per unit area acting in a given point of the fault plane is horizontal if there is a reaction force per unit area (normal stress) σ_r, which is perpendicular to the fault plane (Fig. 2c) and is represented as $\sigma_r = F_l \tan\alpha$; σ_r is positive for a tensional stress. Because of the reaction force introduced in the model, there are no vertical forces acting on the blocks and hence no vertical displacement of the blocks.

The interaction of a rigid block with the underlying medium (e.g., the lower ductile crust) takes place along the block bottom, and its dynamics of this interaction is described mathematically by the equations similar to Eqs. (1) and (2) with the elastic K_u and inelastic W_u parameters, which are considered to be constant and proportional to the shear modulus and inversely proportional to the viscosity of the underlying medium, respectively.

The components of the translational vectors of the blocks and the angles of their rotation about the geometric centers of the block bottoms are found from the condition that the total force and the total moment of forces acting on each block must vanish. This is the condition of quasi-static equilibrium of the system and at the same time the condition of minimum energy. The equilibrium equations include only forces caused by specified movements of the underlying medium and of the boundaries of the block-and-fault structure. In fact, it is assumed that the action of all other forces (e.g. gravity) on the structure is ruled out and does not cause displacements of blocks.

The space discretization required to carry out numerical simulations of the BAFD model is made by splitting the faults, on which the forces act, into small cells of trapezoidal shape, whose linear size does not exceed a specified parameter χ. The coordinates (X, Y), displacement $\Delta = (\Delta_t, \Delta_l)$, inelastic displacement $\delta = (\delta_t, \delta_l)$, and elastic normal stress σ_r are supposed to be the same for all the points of a cell.

2.2. Synthetic earthquakes

Earthquakes are simulated using the criterion of the Coulomb failure stress and the dry friction law. For each cell of the fault plane, we introduce the dimensionless number

$$\kappa = \frac{|\mathbf{F}|}{P - \sigma_r}, \tag{4}$$

where $|\mathbf{F}|$ is the magnitude of the shear stress along the fault plane, and P is the difference between the lithostatic and pore (hydrostatic) pressure in the fault zone, which is assumed to be equal to 2×10^8 Pa (the typical value at 15 km depth) for all model faults. The initial conditions for the BAFD model are assumed to satisfy the inequality $\kappa < B$ for all cells of the fault planes, where B is the coefficient of friction specified for each fault segment. In the modeling, we assume $B = 0.3$ for all fault segments. If at any time the value of κ exceeds the level B at one or more cells, a failure (earthquake) occurs, so that κ drops to 0.25 (e.g., Reasenberg and Simpson, 1992; Iio, 1997).

An earthquake in the model is defined as an abrupt increase of the inelastic displacement δ in the cell. The inelastic displacement is updated after the failure using Eqs. (2) and (3). Once the new values of the inelastic displacements for all failed cells are computed, the translation vectors and the angles of rotation of the blocks are computed to satisfy the condition of the quasi-static equilibrium. If after these computations

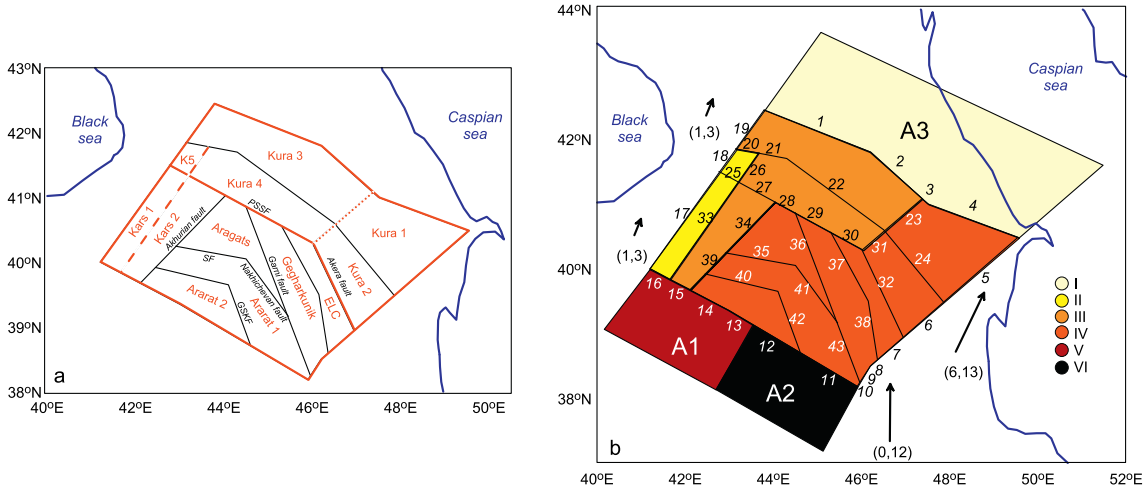

Fig. 3. Geometry of the BAFD model structure for the Transcaucasia region. (a) Block and faults with their names. ELC: the Eastern Lesser Caucasus block; K5: the Kura 5 block; PSSF: the Pambak-Sevan-Sunik fault; SF: the Sardarapat fault; and GSKF: the Gailatu - Siah Cheshmeh - Khoy fault. Model fault segments with parameter $W_0 = 0.001$ (black), $W_0 = 0.002$ (solid red), $W_0 = 0.0002$ (dashed red), and $W_0 = 0.02$ (dotted red). (b) The rates of motion at the bottom of the crustal blocks (in colors), and the values are in Table 2. The boundary velocities are marked by arrows (based on geodetic observations). Numbers in italic are the numbers of fault segments. A1, A2, and A3 mark the boundary blocks. (For interpretation of the references to color in this figure legend, the reader is referred to the web version of this article.)

$\kappa > B$ for some cell(s) of the fault planes, the procedure is repeated for the this(these) cell(s); otherwise, the numerical simulation is continued in the ordinary way.

We note that within inter-seismic periods the rate of inelastic displacements is small and almost constant, and hence the model with a nonlinear fault slip does not much differ from the model with a linear slip. When an earthquake occurs, however, this rate increases significantly (according to Eq. (2)) resulting in lowering effective viscosity. During further simulations, the rate of inelastic displacement decreases gradually and the viscosity return to its normal values (as before the earthquake).

On the same fault segment, a connected cluster of the cells, in which failure occurs at the same time, forms a single earthquake. The magnitude of the earthquake is estimated using the empirical relationship between the magnitude and source area:

$$M = D_1 \log_{10} S + D_2, \quad (5)$$

where S is the total area of the cells forming the earthquake, measured in km^2. The parameter $D_1 = 0.98$ and $D_2 = 4.07$ (Wells and Coppersmith, 1994). We note that the minimum magnitude of the synthetic earthquakes is constrained by the size of the cell used for space discretization of the model fault segments.

Finally, to simulate earthquakes in the BAFD model the following inputs should be introduced: (i) the geometry of crustal blocks, the block's thickness, the dip angle of each fault separating the blocks, and the size of the cell discretizing fault segments; (ii) the driving forces, namely, the velocity of the motion (e.g. determined from geodetic measurements) at the lateral confining boundaries of the model and the velocity at the bottom of the block structure; (iii) rheological parameters of the faults and the bottom of the block structure; and (iv) the criteria (parameters) for earthquake occurrences and the fault slip. The model outputs are the earthquake catalog, focal mechanisms, velocities of blocks, and fault slip rates. The output data allow to analyze earthquake clustering, occurrence of large seismic events, spatial-temporal correlation between earthquakes, mechanism of earthquakes, seismic moment release and some other features of seismicity and tectonic motions. We refer readers to Soloviev and Ismail-Zadeh (2003) and Ismail-Zadeh et al. (2018; Appendices A and B) for more details of the BAFD model.

2.3. Model limitation

As any model, the BAFD model cannot and does not aim to reproduce observed regional seismicity patterns in full details, but basic features of the seismicity, especially large seismic events, which are likely to be related to an existing fault structure. The model has several limitations and uncertainties, which we discuss below. Lithospheric plates are considered in the model to be rigid, however, depending on time scales and stress-loading conditions, the lithosphere may exhibit more complex rheological behavior including elastic, brittle and viscous properties.

Rigid blocks employed in BAFD models allow reproducing a long-range interaction of seismicity and clustering of seismic events, although in real seismicity the earthquake interaction and clustering can be not so well pronounced as in the models. Directly related to the rigidity of lithospheric blocks, the BAFD model assumes no changes in the geometry of blocks and faults during numerical simulations, which can be valid for short time scales. Also, the model does not consider the heterogeneity of the lithosphere and its depth variation.

Another model assumption is that the width of fault zones (areas of strain accumulation), which could range from several meters to km. Meanwhile, in the BAFD model, fault segments are considered to be infinitely thin planes. This assumption is in a good agreement with some field observations and theoretical modeling suggesting that slip in individual seismic events may be extremely localized and occur primarily within a thin shear zone of less than a few mm (e.g., Rice, 2006). Also, the model assumes that strain and stress are localized in the fault segments. It is justified by the fact that the effective elastic moduli and effective viscosity of fault zones are significantly smaller than those within the lithospheric blocks (e.g. Hacker et al., 1992; Fialko, 2006; Barbot et al., 2009), and hence strain localization in the fault zones is higher than that within lithospheric blocks.

3. Blocks-and-faults structure model geometry for Transcaucasia

The BAFD model structure has been developed for the Transcaucasian region and its surroundings on the basis of the block structure model by Karakhanian et al. (2013), geomorphological zoning model by Soloviev and Gorshkov (2017), active fault structure (Trifonov et al., 1994; Avagyan et al., 2010), and spatial distribution of earthquakes and GPS velocities (e.g., Reilinger et al., 2006; Djamour

et al., 2011; Karakhanian et al., 2013; Kadirov et al., 2015). The model structure geometry is presented in Fig. 1 and Fig. 3 (in some detail).

The Kura depression with the adjacent region is split into five blocks (Kura 1 to Kura 5). The Lesser Caucasus region is divided into Aragats, Gegharkunik, the Eastern Lesser Caucasus (ELC), and the Ararat blocks. The Ararat block itself is split into Ararat 1 and Ararat 2 blocks along the system of faults Gailatu–Siah Cheshmeh–Khoy (GSKF) (Djamour et al., 2011), where at least two historical M7+ and several M6+ earthquake occurred. The Kars block is divided into Kars 1 and Kars 2 blocks along a seismically active lineament. Although the blocks are considered in the model to be perfectly rigid, we recognize that blocks bounded by thrust (or normal) faults shrink (or stretch) during geological times, but their deformation for the time of several thousand years is insignificant compared to the block sizes.

The blocks representing geological structural element of the region compose the core structure of the BAFD model. To avoid the determination of conditions at rigid immobile lateral boundaries of the structure (to the north-east and south-west of the model blocks), three additional blocks A1 and A2 (of the Turkish-Iranian Plateau), and A3 (of the Greater Caucasus and the adjacent Caspian Sea) are introduced in the model as boundary blocks (Fig. 3b). These blocks do not correspond to real geological structures, and hence $K = 0$ is specified for the outer fault segments of the blocks (assuming no stress at these segments).

Thus, the model structure contains 15 blocks in total and 43 segments of fault planes (Fig. 3b). The faults in the BAFD model structure do not trace exactly the regional faults, but rather represent the main geometrical features of the regional fault system. For example, one of the major faults crossing the region along the Lake Sevan is the Pambak-Sevan-Sunik fault (PSSF) system. The Garni fault joints the PSSF system zone forming a structure of young ruptures including the rupture of the Spitak earthquake. Although both the PSSF and the Garni fault are included in the BAFD model, the model structure does not contain the young rupture surfaces located in the close vicinity to segment 28. Similarly, the model fault segments do not exactly trace the rupture zones of the Shamakha earthquakes and the Racha earthquake, and these earthquakes are associated with model fault segments 4 and 1, respectively.

Dip angles of the fault planes in the model are estimated from earthquake focal mechanisms and structural schemes and cross-sections (Avagyan et al., 2010). The dip angle of 45° is prescribed to fault segments along the northeastern boundary of the model domain separating the Kura basin from the Greater Caucasus as well as to the PSSF and the Akera fault. The dip angle of the fault segments at the outer northwestern, southeastern and southwestern boundaries of the model domain is 70°. Dip angle of 85° is prescribed, when either the fault planes are nearly vertical or there is no information on the dip angle.

The shallow nature of observed earthquake foci (with an exception for the intermediate-depth earthquakes observed beneath the eastern part of the Greater Caucasus; Mumladze et al., 2015) suggests that the upper crust is thin and underlain by a ductile layer. We consider that the average thickness of the rigid crustal blocks is 30 km, and assign $H = 30$ km between the upper and lower planes (boundaries) of the model structure. We should note that the thickness of the rigid crustal blocks influences seismicity parameters, such as the earthquake magnitude and the number of events. The maximum magnitude drops with the decreasing thickness of the rigid blocks as the magnitude is proportional to the size of a rupture's area. The rupture areas are normally smaller in the thin crust than in the thick one, and hence the maximum magnitude of synthetic seismic events becomes smaller. Numerical experiments show that with decreasing thickness of the crustal blocks by 10 km, the maximum magnitude of synthetic events drops by 0.1–0.2, and vice versa, with the increase of the thickness, the maximum magnitude and the number of earthquakes increase. Meanwhile, the spatial pattern of seismicity does not change significantly with the varying upper crust's thickness.

The following values are prescribed to the parameters of the BAFD model in our numerical experiments. The elastic parameter $K = K_u = 1$ corresponding to the shear modulus 3×10^{10} Pa is assumed to be the same on all fault segments and the block bottom planes. The inelastic parameter $W_u = 0.001$, which corresponds to viscosity 3.15×10^{20} Pa s, is also constant except in the case of experiments 7 and 8. Parameter W_0 differs with fault segments: $W_0 = 0.002$ at the fault segments of the outer model boundary as well as at the PSSF and the Akera fault; $W_0 = 0.0002$ at the lineament separating blocks Kars 1 and Kars 2; and $W_0 = 0.02$ at the model segments separating blocks Kura 1 and Kura 3 as well as Kura 2 and Kura 4. The higher W_0 value is assigned to these Kura segments as low seismic activity is observed on the segments, but the GPS velocities are higher in blocks Kura 1 and Kura 2 compare to those in blocks Kura 3 and Kura 4. At other internal fault segments $W_0 = 0.001$. The values of the parameters for the time and space discretization are $\Delta t = 10^{-2}$ y and $\chi = 2$ km, respectively. The values of the parameters specified here are default values in all numerical experiments (if other values of the parameters are not prescribed).

Total displacements of the blocks are represented by their translations along the X and Y axes of the reference coordinate system and by the angles of rotation around their geometrical centers. The point with the geographic coordinates 40.5° N and 45° E is chosen as the origin of the reference coordinate system. The X-axis is the east-oriented parallel passing through the origin of the coordinate system; the Y-axis is the north-oriented meridian. The model driving forces (that is, the boundary velocities) are prescribed according to the GPS velocities (Vernant and Chery, 2006; Djamour et al., 2011; Karakhanian et al., 2013; Kadirov et al., 2015). The vector velocity (1, 3) mm yr^{-1} is prescribed at the western and northwestern boundaries of the model, (6, 13) mm yr^{-1} at its eastern boundary, and (0, 12) mm yr^{-1} at its southeastern boundary (see Fig. 3b). As a motion of the lower crust may not exactly mimic the surface motion, the motion of the ductile lower crust (that is, the medium underlying the rigid crustal blocks in the model) and the coupling between the upper and lower crust are subject to numerical investigations (in sects. 4.4 and 4.5, respectively). We assume in the model that the azimuth of the default orientation of the motion of the underlying medium is 26° with respect to the north; that is, the underlying medium moves with the velocity (V_x, V_y), where $V_y = 2V_x$. The movement velocities of the block groups I to VI are shown in Table 2 (as for experiment 1) and Fig. 3b.

The numerical simulations were performed for 20,000 (20K) years starting from zero initial conditions, and some time is needed for quasi-stabilization of deviatoric (tectonic) stresses. The stabilization time can be estimated from the time-magnitude histogram (e.g., Soloviev and Ismail-Zadeh, 2003). We estimated the stabilization time for the studied models to be about 10K years, and therefore, our analysis and interpretations cover the period of time from 10K to 20K years.

4. Numerical results

Some parameters of the BAFD model can be determined from direct observations and measurements (e.g., the geometry of the blocks, active faults and lineaments, GPS velocities). Other parameters of the model are less known (e.g., the rate of movement of the lower crust, coupling

Table 2
Velocity (V_x, V_y), in mm y^{-1}, of the underlying medium's movement.

Model region	Experiment 1		Experiment 3		Experiment 4	
	V_x	V_y	V_x	V_y	V_x	V_y
I	0	0	0	0	0	0
II	1.5	3.0	0	3.35	2.37	2.37
III	3.0	6.0	0	6.71	4.74	4.74
IV	4.5	9.0	0	10.06	7.12	7.12
V	−5.0	15.0	−5.0	15.0	−5.0	15.0
VI	−2.0	15.0	−2.0	15.0	−2.0	15.0

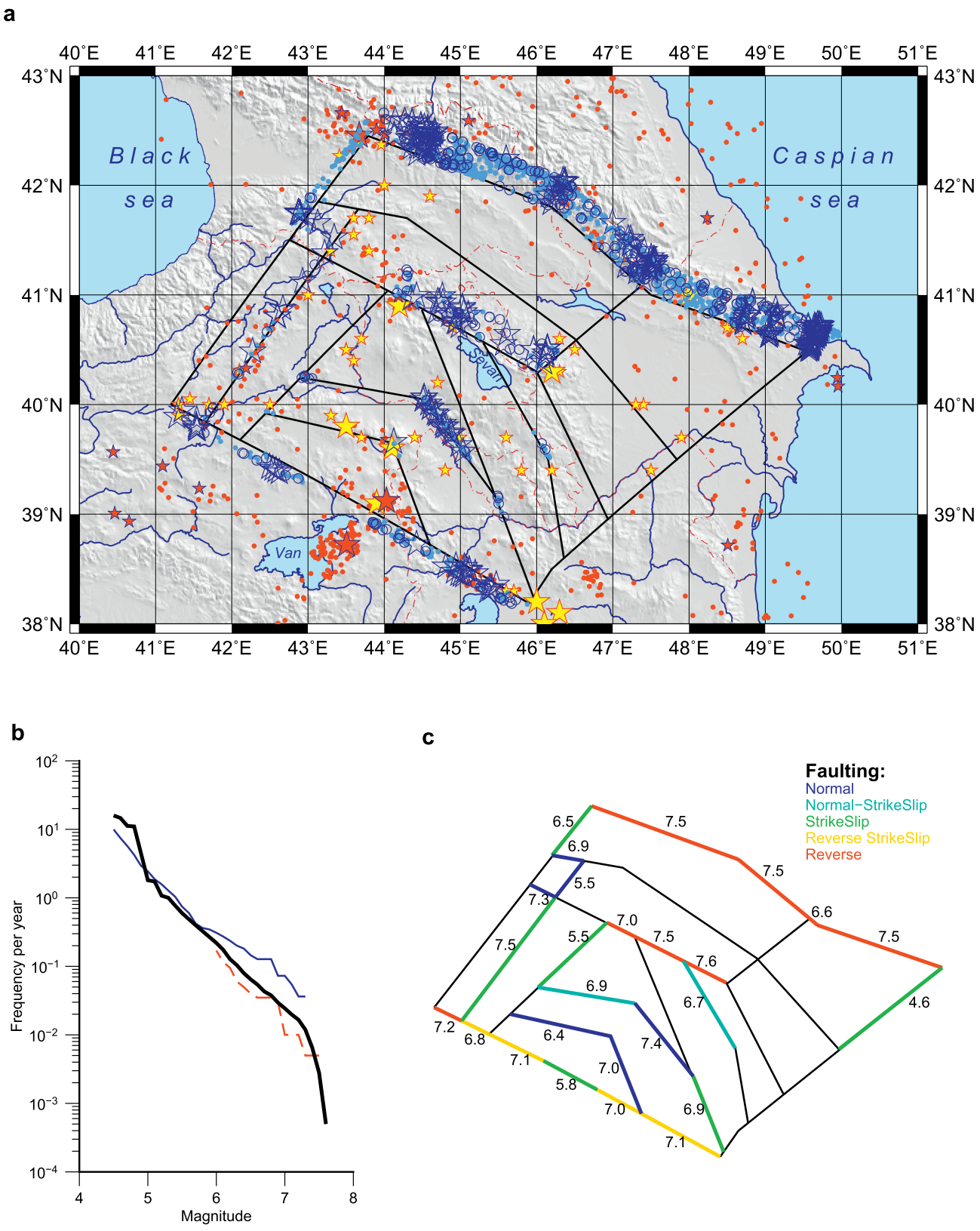

Fig. 4. Synthetic seismicity in *experiment 1*. (a) Distribution of synthetic seismicity (with earthquake magnitudes > 6) imposed on the map of observed seismicity: blue stars mark earthquakes of magnitude M7+, blue circles M6.5+ events, and light blue dots M6+ events. (b) The frequency-magnitude curves: black curve corresponds to the synthetic events, and red/blue curves to recorded seismicity (as in the insert of Fig. 1). (c) Focal mechanisms of synthetic earthquakes on the faults (indicated by fault segment's colors) and the maximum magnitude of synthetic earthquakes on each fault segment (marked by the number at the segments). Black segments denote no synthetic earthquakes. (For interpretation of the references to color in this figure legend, the reader is referred to the web version of this article.)

between the blocks and the lower crust, rheology of the fault segments). Therefore, we have developed a number of experiments to clarify the influence of less known parameters on the seismicity of the studied region (e.g., Ismail-Zadeh et al., 1999, 2007). The numerical experiment, which is most consistent with seismic observation in the Transcaucasian region, is presented in sub-sect. 4.1. We analyze then how the seismic pattern, earthquake magnitudes and their mechanisms in the model are influenced by the following factors: linear versus nonlinear fault slip (sub-sect. 4.2); variations in the movement of the lower crust (sub-sect. 4.3); changes in the inelastic properties of the fault zones (sub-sect. 4.4); and coupling with the lower crust (sub-sect. 4.5).

4.1. Preferred model

We present here the model experiment, which is most consistent with the following observations on the seismic activity of the Transcaucasian region (and refer to this experiment as 'preferred' or *experiment 1*): earthquake frequency versus magnitude (FM curve), spatial distribution of the earthquakes, and their mechanisms. The pattern of seismic events in the preferred experiment reveals features of observed seismicity (Fig. 4a). The *b*-value and the earthquake productivity reflected in the FM curve (Fig. 4b) for observed (recorded) and the synthetic events are in a good agreement. The focal mechanisms of synthetic seismicity confirms general patters of the regional stress state (Fig. 4c; also Fig. S1 in the Supplementary material).

The areas, where strong earthquakes occurred in the past, have been reproduced as areas of strong synthetic seismicity by this model experiment. Fig. 5 presents earthquake sequences at specific model fault segments. Fault segment 1 (see the segment numbers in Fig. 3b), where the 1991 Mw7.0 Racha (Georgia) earthquake had occurred, produces synthetic earthquakes of magnitude 7+ (with the maximum magnitude of 7.5; Fig. 4c) with a reoccurrence time of about 300 years. We note that although the existing historical data do not show earthquakes of magnitude 7+ on the fault before the 1991 Racha earthquake, the historical data may be incomplete. Fault segment 4, which was the site of strong earthquakes in Shamakha (Azerbaijan) in 1667 (M7.8), in 1859 (M6.5), and in 1902 (M6.9 ± 0.2), produces also earthquakes of magnitude 7+ (with the maximum magnitude of 7.5) with a reoccurrence time of about 200 years. Model segment 28, which is associated with rupture zone the 1988 Mw6.9 Spitak (Armenia) earthquake (Cisternas et al., 1989), produces strong synthetic earthquakes (of magnitude 6.5+) quite rare in the model experiment with reoccurrence time of about 1000 years.

The model experiment shows that segments 1, 2, and 4 associated with the foot of the Greater Caucasus mountains ruptures quite often in the model (producing many earthquakes with magnitude > 6), releasing significant energy due to the convergence between the Arabian and Eurasian plates, when compared to segments 28–30 crossing the northern Lesser Caucasus, where smaller seismic events cluster either prior a bigger event or in-between bigger events. All synthetic earthquakes at fault segments 1, 2, 4, and 28–30 show the thrust-fault mechanism in agreement with the observed regional stress state (e.g., Tan and Taymaz, 2006; Ritz et al., 2016).

Fault segments 11 and 12, representing the southern boundaries of model blocks Ararat 1 and Ararat 2, 'synchronize' the times of strong (M6.5+) earthquakes (see Fig. 5), and the reoccurrence time of the earthquakes at the segments is about 600 years. This 'synchronization' suggests that both segments can rupture simultaneously generating events of higher magnitude. Focal mechanisms of synthetic earthquakes are strike-slip to reverse-strike slip, consistent with the focal mechanism of the 1976 Turkey-Iran border M7.3 earthquake occurred in the area.

Another area of observed M6+ seismicity is associated with fault segment 33 to the southeast of the Black Sea. The model reoccurrence times of M6+ and M7 +events are about 350 years and

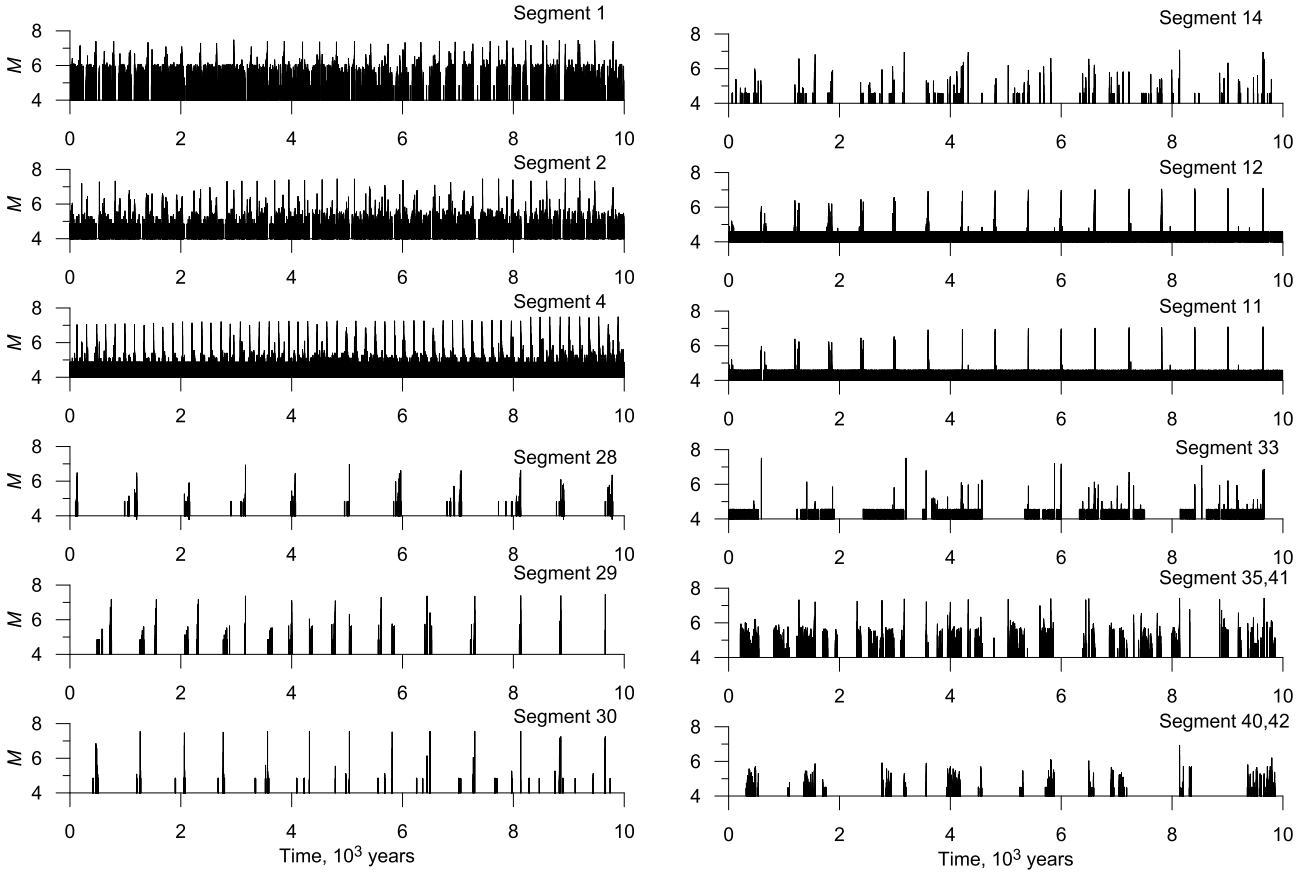

Fig. 5. Seismicity in *experiment* 1 showing earthquake magnitudes versus time for individual fault segments.

Table 3
Reoccurrence time of strong (M ≥ 6.0) earthquakes in numerical experiments.

Segment #	Average reoccurrence time in years / magnitude of seismic events			
	Exp. 1 (see Fig. 5)	Exp. 2 (see Fig. 9)	Exp. 3 (see Fig. S3)	Exp. 4 (see Fig. S5)
1	300/7.0+	700/6.0+	650/7.0+	160/7.0+
2	450/7.0+	No M6 events	1250/7.0+	300/7.0+
4	200/7.0+	No M6 events	100/7.0+	2000/7.0+
11	650/6.0+	500/6.0+	–	5000/6+
12	650/6.0+	650/6.0+	–	5000/6+
14	650/6.0+	5000/6.0+	–	160/6+
28	900/6.0+	800/6.0+	10,000/6.0	750/7.0+
29	800/7.0+	700/7.0+	5000/6.0+	750/7.0+
30	800/7.0+	650/7.0+	1600/6.0+	750/7.0+
33	2000/7.0+	900/6.0+	–	650/7.0+
35, 41	650/7.0+	1000/7.0+	1600/7.0+	–
40, 42	2000/6.0+	2000/6.0+	750/6.0+	–

1500–2000 years, respectively. Also, the numerical experiment has showed that segment 41 (modeling the Nakhichevan fault) and segment 42 (modeling GSKF) experience normal faulting earthquakes of maximum magnitude 7.4 (reoccurrence time of about 700 years) and 6.9 (very rare), respectively. The reoccurrence time of the strongest events in experiment 1 is summarized in Table 3.

The results of the numerical experiments based on the BAFD model allow us to interpret the contemporary movements in Transcaucasia as motions of rigid upper crustal blocks driven by the north-northeastward indentation of Arabian plate into Eurasia and a motion of the lower crust. The fault slip rates, calculated as a ratio of the fault slip during the entire model time (10K years) to this time, are presented in Fig. 6. The total displacement rate of the model blocks and their interseismic and coseismic components are presented in Table 4 and Fig. 7.

4.2. Linear versus nonlinear fault slip

To analyze how the nonlinear slip rate influence the distribution of earthquake in space, time and magnitude in the model, we consider here the case of a linear viscoelastic slip at faults and have performed a numerical experiment (*experiment 2*) assuming the power-law exponent $n = 1$ in Eq. (3). The spatial distribution of seismic events in this experiment is illustrated in Fig. 8a, FM curves for the observed and synthetic events in Fig. 8b, and focal mechanisms and maximum magnitudes at the fault segments in Fig. 8c. The model results show that no strong (M6.5+) seismicity is produced on fault segments 1, 2, and 4, and the seismic energy is scattered over a significant number of smaller

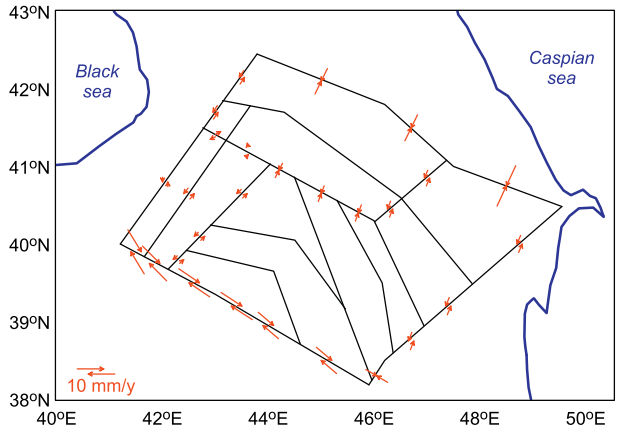

Fig. 6. Fault slip rates in *experiment* 1. The rates smaller than 0.3 mm y^{-1} are not shown here. The symbols (arrows) mark three types of major fault slips: strike-slip (two parallel converging arrows), thrust dip-slip (two aligned arrows with the adjacent heads), and normal dip-slip (two parallel diverging arrows).

magnitude earthquakes (Fig. 9). Hence, this synthetic seismicity pattern does not support the observed seismicity pattern at the fault segments, where Racha and Shamakha earthquakes occurred. Nevertheless, strong (M7+) synthetic earthquakes are generated on segments 28–30, 33, and 41as well as on segments 8–10, where some historical strong events occurred. Meanwhile, the frequency-magnitude relationship for synthetic events does not match well that of observed seismicity (Fig. 8b): the number of earthquakes with the magnitude range between 5.5 and 6.5 much lower that observed, and the number of smaller ($M < 5$) synthetic events is bigger by about an order of magnitude. The productivity of earthquakes can be improved by tuning the model rheological parameter W_0 for individual faults, but this was not the aim of this experiment.

4.3. Variations in the movement at block's bottom

In the preferred numerical experiment, the model blocks move in the NNE direction (with the azimuth 26° with respect to the north) according to the geodetic observations related to the main part of the model domain (Fig. 1), and the movement is prescribed in the model to the bottom of the blocks. Meanwhile the movement of the block's bottoms is unknown in detail, and therefore, in this sub-section, we analyze how the orientation of this movement influences the distribution of seismicity by varying the azimuth from 0° (the movement to the north) to 45° (the movement to the northeast). The rates of the movement are presented in Table 2 for different experiments. All other model parameters in the experiments are the same as in the preferred experiment.

Movement to the north (*experiment 3*). Compared to the results of *experiment 1*, the spatial distribution of seismic events is altered considerably in *experiment 3*. Although the strong events (up to M7.7) are generated along the northern boundary of the model (fault segments 1–4), the significant number of strong synthetic events occur along the northeast boundary (segment 5), no events occur on southern (segments 11 to 16) and southwestern (segment 33) boundaries. No strong synthetic seismicity is generated at internal fault segments 27–30, and the number of strong events is reduced on segment 41 in the model (Figs. S2a,c; S3; note that figures related to *experiments 3–8* can be found in the Supplementary material). Meanwhile, the frequency-magnitude curve does not much differ from that in *experiment 1* for the earthquakes of magnitude > 6, while the number of smaller magnitude events increase significantly (Fig. S2b). Compared to *experiment 1*, more normal to strike-slip events occur in this experiment (Fig. S2c).

Movement to the northeast (*experiment 4)*. In this experiment, the spatial distribution of seismic events differs from that in *experiments 1* and *3*. Although strongest events are still associated with the northern boundary of the model, seismic events at segment 2 are significantly less (Fig. S4a). Strong seismic events (up to M7.5) occur now on fault segments 17–19 of the western model boundary, which have not been observed in this part of the region for the last several centuries. Meanwhile, lower magnitude seismic events are obtained on the southern segments (12–16) of the model domain with no strong seismicity at segment 11. The magnitude of earthquakes at segments 28–30 are still high (up to 7.6) and the reoccurrence time is about 750 years, but the large events are singular at the fault segments and do not accompany by smaller-size events (see Fig. S5). At the same time, the FM curve does not differ significantly from that in *experiments 1* and *4* for the earthquakes of magnitude > 6, although the number of smaller magnitude events is higher compared to the same experiments (Fig. S4b). In experiments 1, 3, and 4, the mechanisms of strong synthetic events show stability at the northern and southern boundaries of the model domain as well as at segments 28–30 (Fig. S4c).

4.4. Influence of the rheology of fault segments on seismicity

In numerical experiments, a specific value of the inelastic parameter

Table 4
Total, interseismic, and coseismic block displacement rates in experiment 1.

Block	Total			Interseismic			Coseismic		
	V_{xt}, mm y^{-1}	V_{yt}, mm y^{-1}	ω, 10^{-6} rad y^{-1}	V_{xt}, mm y^{-1}	V_{yt}, mm y^{-1}	ω,10^{-6} rad y^{-1}	V_{xt}, mm y^{-1}	V_{yt}, mm y^{-1}	ω, 10^{-6} rad y^{-1}
Kars 1	1.041	4.607	0.019	1.499	5.671	0.007	−0.458	−1.065	0.012
Kars 2	2.724	6.854	0.019	2.504	6.990	0.008	0.220	−0.135	0.010
Ararat 1	4.563	8.699	0.026	4.128	8.742	0.027	0.435	−0.043	−0.002
Ararat 2	4.527	8.468	0.027	4.006	8.558	0.037	0.520	−0.089	−0.010
Aragats	4.380	8.573	0.022	4.020	8.542	0.018	0.360	0.031	0.003
Gegharkunik	4.392	9.152	0.021	4.151	8.769	0.021	0.241	0.383	0.000
ELC	4.368	9.321	0.021	4.132	8.892	0.022	0.236	0.429	−0.001
Kura 1	4.353	9.338	0.017	3.638	8.250	−0.010	0.716	1.088	0.027
Kura 2	4.384	9.296	0.017	3.569	8.395	−0.006	0.816	0.901	0.023
Kura 3	2.882	5.879	0.009	2.574	5.231	0.002	0.308	0.648	0.007
Kura 4	2.907	5.853	0.009	2.482	5.322	0.004	0.425	0.531	0.005
Kura 5	2.844	5.719	0.010	2.428	5.224	0.001	0.416	0.495	0.009

$V_t = (V_{xt}, V_{yt})$ is the velocity of translational motion, and ω is the angular velocity of rotational motion of rigid blocks.

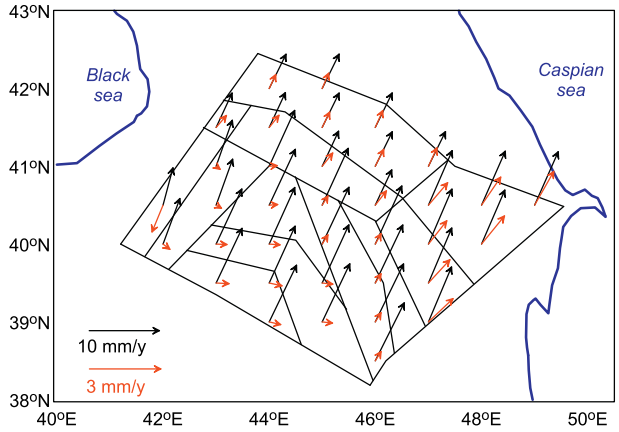

Fig. 7. Block displacement rates in *experiment* 1. Black and red arrows mark interseismic and coseismic displacements, respectively. (For interpretation of the references to color in this figure legend, the reader is referred to the web version of this article.)

W_0 was assigned to each fault segment as described in sect. 3, and these values have been kept constant during all previous experiments. In this sub-section, we explore the influence of the inelastic parameter on the distribution of seismicity in the model, and assume that the value W_0 is the same for all fault segments and equals 0.001 (*experiment 5*) and 0.002 (*experiment 6*). All other model parameters are the same as in experiment 1.

In both *experiment 5* (Fig. S6a) and *experiment 6* (Fig. S7a), seismicity pattern changes significantly and looks quite unrealistic compared to the seismicity pattern of the last two centuries. No events of M > 6.1 is obtained on segment 1, where the Racha M = 7 earthquake occurred in 1991 as well as on segment 4, where the Shamakha M = 6.9 ± 0.2 earthquake occurred in 1902, and on segment 28, where the Spitak M = 6.9 earthquake occurred in 1988 (Figs. S6c and S7c). Although strong (M > 7) seismic events still exist at fault segments 16 (with thrust faulting mechanisms) and 25 (with normal faulting mechanisms) as in the case of experiment 1, no strong synthetic seismicity is obtained on seismically active segment 33 (with strike-slip mechanisms) and segments 11–15 (Figs. S6c and S7c).

The FM curves (Figs. S6b and S7b) related to synthetic seismicity obtained from both experiments show that the number of small and moderate events increased significantly and the number of strong events decreased. For example, in *experiment 5*, there are only 29 seismic events of magnitude 7 and greater, 86 events of M6.5+, and 284 of M6+. The higher inelastic parameter W_0 (*experiment 6*), the lower viscosity and the easier fault slip resulting in the increasing number of small events and the decreasing number of larger events. In *experiment 6*, only 13 seismic events have the magnitude > 7, 18 events M6.5+, and 340 events of M6+.

4.5. Coupling with the lower crust

In all previous experiments, we assume that $W_0 = 0.001$ at the bottom of the model blocks. Here we assume that the coupling of model blocks with the underlying medium is weaker ($W_0 = 0.01$ in *experiment 7* and $= 0.003$ in *experiment 8*) keeping the same all other parameters of the model. Assuming that the model blocks represent the upper crust underlain by the lower crust, a weak coupling means a reduction in traction forces and a decrease of the effective viscosity at an interface layer between the lower and upper crust.

In *experiment 7*, the weaker coupling yields to a significant reduction of earthquake productivity (Fig. S8). With an exception of one earthquake of magnitude 7.2 on fault segment 1, the number of strong (magnitude M6+) seismic events in *experiment 8* dropped by about one to two orders of magnitude. Namely, the model generates only 12 events of magnitude > 6.5, and 88 events of magnitude M6+. In *experiment 8*, also the number of stronger earthquakes decreases compared to that in *experiment 1*, but the number of earthquakes of magnitude 5 to 6 increases (Fig. S9). 25 earthquakes of magnitude M7+ obtained occurred on segments 1, 4, 25, and 33; 358 seismic events of M6.5+ and 928 events of M6+ were generated in *experiment 8*. In both experiments, the FM curves of synthetic seismicity are not in the agreement with the frequency-magnitude relationship for observed seismicity with significant numbers of small events and small numbers of the events of M5+.

5. Discussion

The results of the preferred numerical experiment are discussed here in comparison with other experiments and observations. The model results show a good agreement with the properties of the regional seismicity: the magnitude-frequency relationship of modeled seismicity fits well that of the observed seismicity. The blocks' movement and fault slip rates obtained from the model satisfy the observations, e.g. GPS-velocities. The sites of strong synthetic seismicity correlate well with those of observed strong earthquakes, and the reoccurrence time of these events are close to that of observed earthquake.

If the movement of the Arabian plate with respect to Eurasia is considered to be the only driving force of the BAFD model, large synthetic events would cluster mainly on the fault segments 11–16, and this movement would fail to transmit enough stress to the interior of the block structure to produce earthquakes on the internal faults, as was shown in the cases of the movement of the Indian plate with respect to

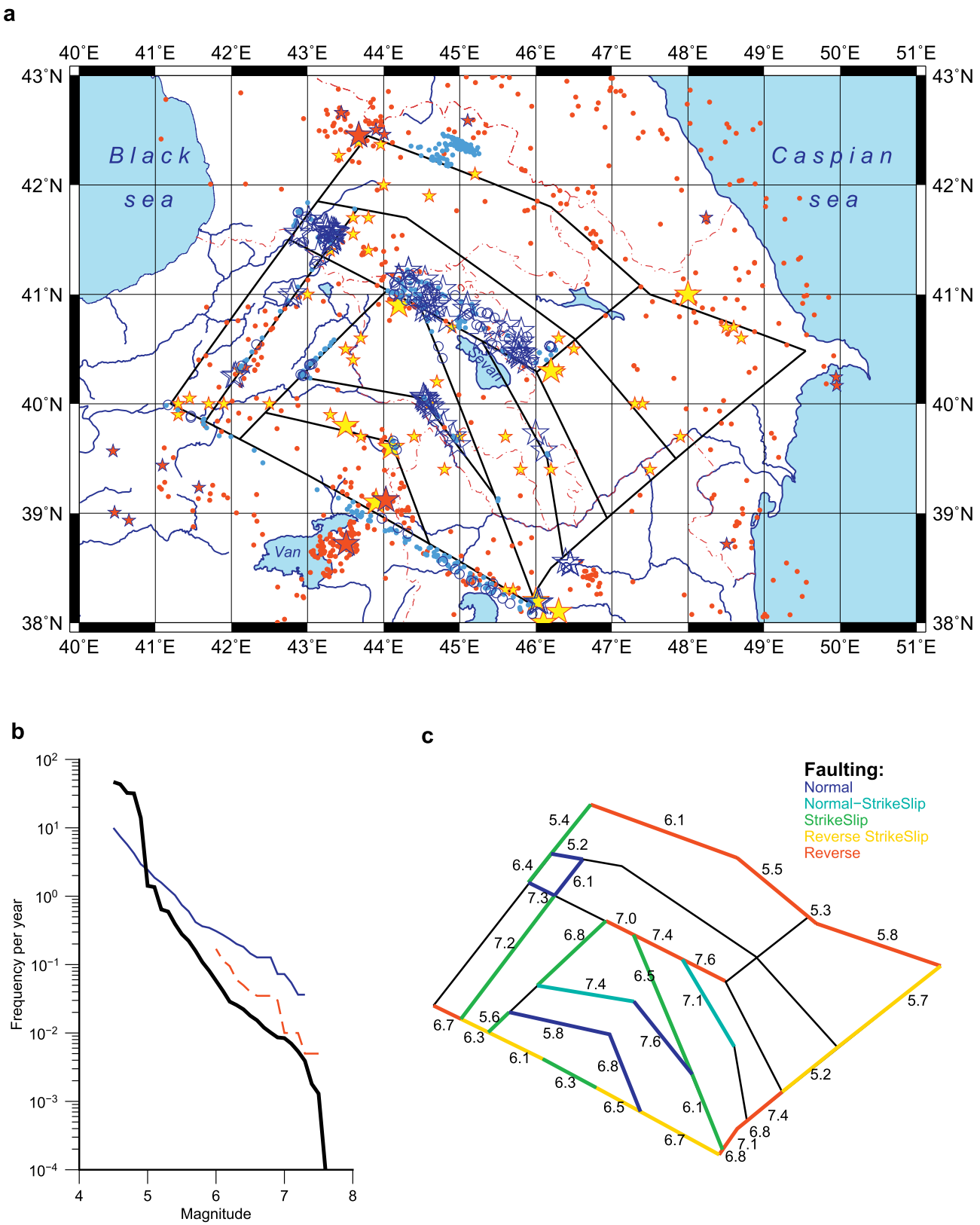

Fig. 8. Synthetic seismicity in the case of *experiment 2* with linear viscoelastic fault slip. (a) Distribution of synthetic seismicity (with earthquake magnitudes > 6) imposed on the map of observed seismicity. (b) The frequency-magnitude curves. (c) Focal mechanisms of synthetic earthquakes and the maximum magnitude of synthetic earthquakes on each fault segment. Notations can be found in the caption of Fig. 4.

Eurasia (Ismail-Zadeh et al., 2007) and the African plate with respect to Eurasia (Peresan et al., 2007). Hence, a coupling of the upper crustal blocks with the underlying lower crust has been introduced in the model. The numerical results demonstrate that the slope of the FM plots and occurrence of strong earthquakes are sensitive to the changes in the movements of the lower crust and to the rheological properties of fault

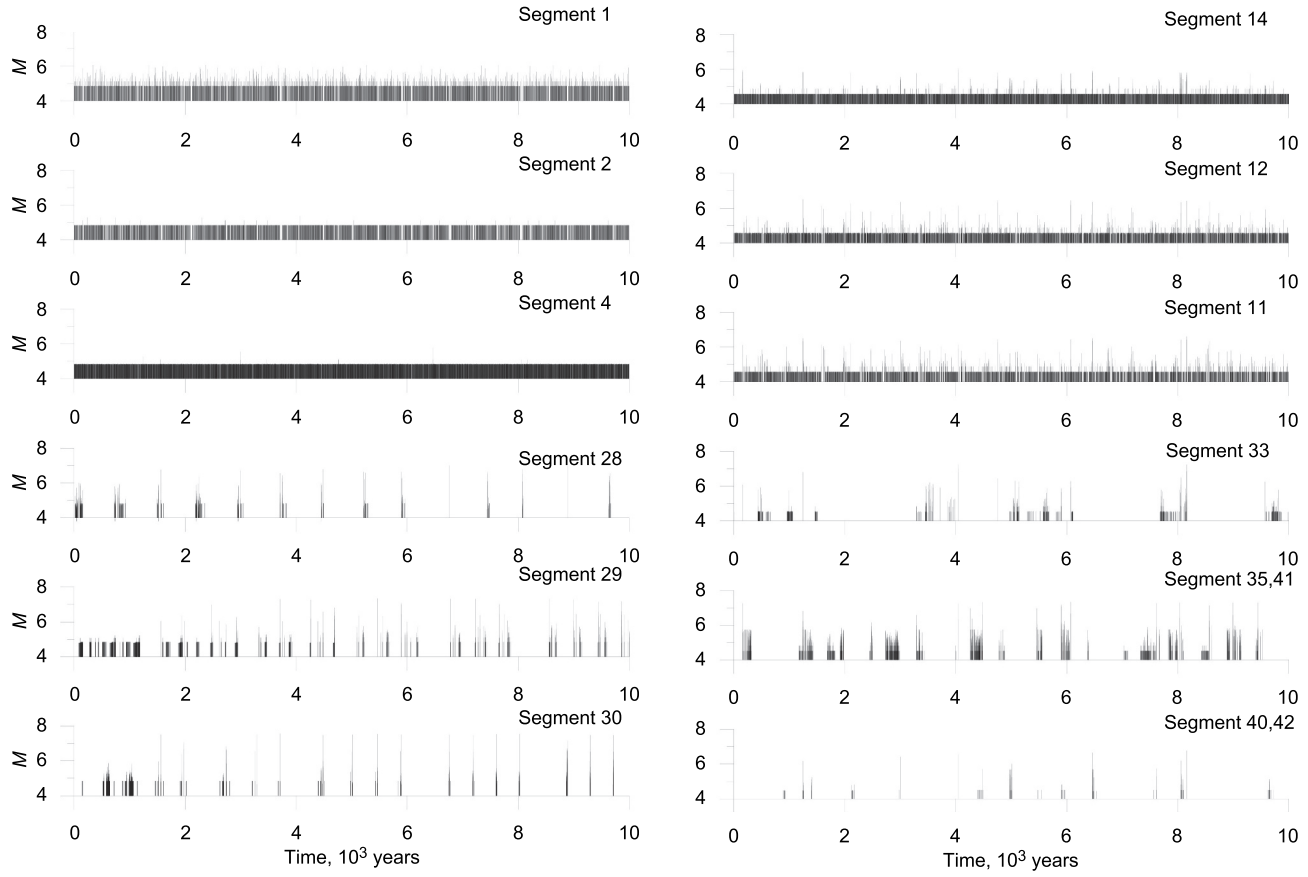

Fig. 9. Seismicity in *experiment* 2 showing earthquake magnitudes versus time for individual fault segments.

plane zones in the region. The movement of the lower crust in the NNE direction well approximate the GPS velocities; strong coupling between the modeled blocks and underlying lower crust provides a better fit to geodetic observations.

The strongest modeled thrust-fault events (M7+) are associated with the foot of the Greater Caucasus mountains and the northern Lesser Caucasus, where strong earthquakes were observed and instrumentally recorded since the 1902 Shamakha earthquake. Based on geomorphological and paleo-seismological investigations Philip et al. (2001) and Karakhanian et al. (2004) showed that the western segment of the PSSF generates strong earthquakes with a long average recurrence time interval of up to 1600 years. Similar behavior exhibits model segments 29 and 30 of the central part of PSSF, but with higher maximum magnitude (up to 7.6) and shorter reoccurrence time of 750 years. Meanwhile, Karakhanian et al. (2004) argue that M > 7.0 events may occur on these segments quite rare with the estimated reoccurrence time of about 4000 years. We note that the last strongest historical event of magnitude 7.5–7.7 (associated with the model fault segment 30) occurred in 1139 (Nikonov and Nikonova, 1986).

Earthquakes of magnitude > 7 (M7+) in the model are also associated with the Nakhichevan fault, where average reoccurrence time of strong modeled seismic events is estimated to be about 650–700 years. Despite the fact that no large events have been observed so far here, if M7+ earthquake happens at the fault in the future, it might present a serious seismic hazard to Yerevan (Armenia) and Nakhichevan (Azerbaijan). Other areas of strong seismicity obtained in the model (but not prominent in the observed regional seismicity) are the central part of the Greater Caucasus (segment 2) and fault segment 14 close to the Van Lake area.

By default, a model rupture occur within a segment as a single earthquake. However, like a natural rupture, the modeled rupture may extend to a neighboring segment. The occurrence of synthetic earthquakes at the same moment of time in one or more neighboring segments suggests at least two possible interpretations of this dynamic behavior: (i) a number of shocks occur on the neighboring segments independently, or (ii) a multi-segment earthquake occurs assuming that the ruptured cells form a connected cluster. Both interpretations are important to be considered in seismic hazard assessments. The magnitude of a multi-segment event can be calculated from Eq. (5) using the joint area of the ruptured cells within the neighboring segments affected (Vorobieva et al., 2017). The maximum magnitude of multi-segment synthetic earthquakes in the southern boundary of the Lesser Caucasus reaches 7.4.

Numerical experiments have shown that the use of the same rheological parameters for all fault segments in the model does not mimic well the regional earthquake pattern, and hence the parameters have been chosen for each fault segment such a way to get a better fit to observed seismicity. The variations in the rheological parameters can be associated with the stress-strain conditions and a presence of fluids. A change in stress and/or in fluid pressure on cracked material of the fault zones will result in a distortion of the cracks, which will alter the effective elastic parameters of the faults zone (Hudson, 2000; Tod, 2002). Also, a presence of water can reduce the viscosity and increase slip rates at faults (Chopra and Paterson, 1984).

The faults along the foot of the Greater Caucasus reveal reverse motions (Fig. 6), which are in agreement with earthquakes fault plane solutions (Fig. 1; Tan and Taymaz, 2006; Ritz et al., 2016). We notice a dominant right-lateral strike-slip on the southwestern outer faults (Karakhanian et al., 2004), while left-lateral motions prevail on the western and eastern outer faults in the model. The Akhurian fault (an inner model fault) shows left-lateral strike-slip motion with a small slip rate of about 1 mm y^{-1}, which is in a good agreement with observations, and fault segments 25 and 27 exhibit normal dip-slip motion compatible with observations (Karakhanian et al., 2004). The observed

fault slip along the PSSF is quite complicated: there are signs of right-lateral strike-slips, but the motions are often associated with a reserve dip-slip (e.g., Philip et al., 2001). The slip rate on the PSSF is estimated from the GPS velocities to be about 2.1 mm y^{-1} (Karakhanian et al., 2013) and from geological studies to be 2.24 ± 0.96 mm y^{-1} (Philip et al., 2001). In the model the PSSF segments exhibits mainly reverse dip-slip with slip rate of about 2 mm y^{-1} consistent with the geodetic and geological estimates.

The modeled interseismic motions have a significant eastward component (Fig. 7) that is in agreement with the regional GPS observations (Fig. 1; Djamour et al., 2011; Karakhanian et al., 2013; Kadirov et al., 2015). We notice that the orientation of block displacement rates during the interseismic phase differs from that of the coseismic phase. If the block velocities for the interseismic phase follow basically the GPS velocities, those, related to the coseismic phase, change their direction depending on the region; namely, the direction of displacement for the coseismic phase: (i) nearly coincides with that for the interseismic phase within Kura 3, Kura 4, Kura 5, ELC, and Gegharkunik blocks, (ii) moves toward the east (by about 30°) within Kura 1 and Kura 2 blocks, and (iii) becomes almost perpendicular (about 80–90° to the east) within Kars 2, Aragats, Ararat 1, and Ararat 2; and (iv) completely change the direction to opposite within Kars 1 block.

The modeled long-term slip rate (displacement velocity) may not fit exactly the GPS velocities determined for a few last decades of geodetic measurements or geological fault slip rates. A difference in fault slip rate/block velocity determinations (apart from possible systematic errors in the GPS or geological estimates) could be explained by model simplifications related to its structure and a short period of GPS observations.

Creep after an earthquake is quite important process leading to elastic stress relaxation. A creep process can be modeled using a viscoelastic rheological law that combines linear elasticity and linear (as in the case of Soloviev and Ismail-Zadeh, 2003) or nonlinear viscosity (as in the case of this work). In the low tectonic stress regime, rocks behaves as a linear viscous fluid and diffusion creep takes place; at higher stresses the motion of dislocations becomes the dominant creep process resulting in a nonlinear (power-law) behavior similar to Eq. (3) (e.g., Turcotte and Schubert, 2002; Ismail-Zadeh and Tackley, 2010).

The rheological behavior of fault zones may change after strong earthquakes. Based on geodetic observations along a subduction zone, Bürgmann et al. (2001) showed that a strong earthquake was followed by rapid aseismic afterslip during about two months, and its moment release was comparable with the earthquake. To control coseismic and postseismic stress drop and afterslip in the linear BAFD model (e.g., Soloviev and Ismail-Zadeh, 2003), two thresholds are introduced and prescribed arbitrarily to obtain a reasonable stress drop after an earthquake. The nonlinear model with a rate-dependent fault slip presented in this work provides gradual decay of the rate of inelastic displacements in the post-seismic period. Therefore, we consider that nonlinear BAFD model provides a better description of seismic processes.

6. Concluding remarks

Dynamics of the lithosphere, representing a complex dissipative system with strong earthquakes for critical transitions, is essentially nonlinear. Two major factors responsible for the complexity are its hierarchical structure extending from tectonic plates to the grains of rocks, and instability caused by a multitude of mechanisms controlling strain and stress localization. A prominent feature of complex systems is the reoccurrence of abrupt overall changes (or so-called critical transitions), and strong earthquakes may be regarded as critical transitions in the lithosphere (e.g., Keilis-Borok, 1990; Turcotte, 1999; Keilis-Borok et al., 2001).

In the case of the BAFD model, a sequence of earthquakes is generated by a network of faults bounding the rigid blocks rather than by a segment of a single fault. Numerical studies of nonlinear dynamics of the lithosphere and earthquake generations have the advantage compared to statistical and phenomenological studies of observed seismicity, because the catalogs produced by earthquake simulations are much larger in the duration of time (up to a hundred thousand years) than the reliable recorded data on earthquakes covering a time interval of < 100 years, which is rather short compared to the duration of tectonic processes responsible for seismic activity (e.g., Ismail-Zadeh et al., 2007, 2018).

The BAFD model provides a tool for studying both deformations (e.g. stress, strain, slip and slip rates) and seismicity (e.g., clustering of earthquakes, relationships between frequency and magnitude of the events, occurrences of strong seismic events). Moreover, the results of numerical modeling of crustal/lithospheric dynamics and earthquake simulations contribute to comprehensive seismic hazard assessments (Sokolov and Ismail-Zadeh, 2015, 2016; Console et al., 2017), providing a better understanding of possible large earthquake occurrences and, hence, allowing for better assessments of ground shaking due to these seismic events. The knowledge of the sites of potential large events may significantly alter the seismic hazard assessment in the region. This is proven for the case of the Tibet-Himalayan region, where the BAFD model determined a zone of large earthquakes (M > 7.5) associated with the Longmen-Shan fault (Ismail-Zadeh et al., 2007), where the destructive Wenchuan (M = 7.9) earthquake occurred in 2008 (a year after the publication of the paper). Seismic hazard assessed in the Tibet-Himalayan region based on the knowledge of the synthetic seismicity (Sokolov and Ismail-Zadeh, 2015) showed a significant difference between the seismic hazard based on additional information from numerical modeling and those assessed by traditional methods.

We have developed the BAFD model of the Transcaucasian region, which incorporates the major regional geological structural elements, and performed numerical experiments addressed to a better understanding of the dynamics of the crustal seismicity and fault slip rates in the region. The main result of the modeling is the identification of zones for potential strong events in the region and their average recurrence times. These localized zones of strong seismicity are associated with the roots of the Greater Caucasus Mountains, PSSF, Nakhichevan fault, and some other regional faults.

The contemporary crustal dynamics and seismicity pattern in the Transcaucasian region and its surrounding are determined by the north-northeastern motion of the Arabian plate relative to Eurasia and the movement of the ductile lower crust overlain by the rigid upper crustal blocks. The number and maximum magnitude of earthquakes change with the variations in the movements of the crustal blocks and in the rheological properties of the underlying lower crust and the fault zones. Variations in rheological properties of the fault zones and/or of the lower crust as well as in the motion of the lower crust influence the regional seismicity patterns. Strong earthquakes and their localization can be considered as a consequence of the dynamics of the crustal blocks and faults in the region.

Acknowledgements

We are thankful to Alexander Soloviev, Birgit Mueller, and Frank Schilling for discussion on earthquake modeling and tectonic stresses in the region. The study was supported by the German Science Foundation (DFG IS 203/4-1) and the Russian Foundation for Basic Research (16-55-12033).

Appendix A. Supplementary data

Supplementary data to this article can be found online at https://doi.org/10.1016/j.pepi.2019.106320.

References

Adamia, Sh., Chkhotua, T., Kekelia, M., Lordkipanidze, M., Shavishvili, I., Zakariadze, G., 1981. Tectonics of the Caucasus and adjoining regions: implications for the evolution of the Tethys ocean. J. Struct. Geol. 3 (4), 437–447.

Adamia, S., Alania, V., Tsereteli, N., Varazanashvili, O., Sadradze, N., Lursmanashvili, N., Gventsadze, A., 2017. Postcollisional tectonics and seismicity of Georgia. In: Sorkhabi, R. (Ed.), Tectonic Evolution, Collision, and Seismicity of Southwest Asia. In: Honor of Manuel Berberian's Forty-Five Years of Research Contributions: Geological Society of America Special Paper 525, pp. 535–573.

Allen, M., Jackson, J., Walker, R., 2004. Late Cenozoic reorganization of the Arabia-Eurasia collision and the comparison of short-term and long-term deformation rates. Tectonics 23, TC2008. https://doi.org/10.1029/2003TC001530.

Avagyan, A., Sosson, M., Karakhanian, A., Philip, H., Rebai, S., Rolland, Y., Melkonyan, R., Davtyan, V., 2010. Recent tectonic stress evolution in the Lesser Caucasus and adjacent regions. In: Sosson, M., Kaymakci, N., Stephenson, R.A., Bergerat, F., Starostenko, V. (Eds.), Sedimentary Basin Tectonics From the Black Sea and Caucasus to the Arabian Platform. Geological Society, London, Special Publications 340. pp. 393–408.

Barbot, S., Fialko, Y., Sandwell, D., 2009. Three-dimensional models of elastostatic deformation in heterogeneous media, with applications to the Eastern California Shear Zone. Geophys. J. Int. 179, 500–520.

Bürgmann, R., Kogan, M.G., Levin, V.E., Scholz, C.H., King, R.W., Steblov, G.M., 2001. Rapid aseismic moment release following the 5 December 1997 Kronotsky, Kamchatka, earthquake. Geophys. Res. Lett. 28 (7), 1331–1334.

Chopra, P.N., Paterson, M.S., 1984. The role of water in the deformation of dunite. J. Geophys. Res. 89, 7861–7876.

Cisternas, A., Philip, H., Bousquet, J.C., et al., 1989. The Spitak (Armenia) earthquake of 7 December 1988: field observations. Seismology and Tectonics. Nature 339, 675–679.

Console, R., Nardi, A., Carluccio, R., Murru, M., Falcone, G., Parsons, T., 2017. A physics-based earthquake simulator and its application to seismic hazard assessment in Calabria (Southern Italy) region. Acta Geophys. 65, 243–257.

Copley, A., Jackson, J., 2006. Active tectonics of the Turkish-Iranian Plateau. Tectonics 25, TC6006. https://doi.org/10.1029/2005TC001906.

Dewey, J.F., Pitman III, W.C., Ryan, W.B.F., Bonnin, J., 1973. Plate tectonics and the evolution of the Alpine system. Geol. Soc. Amer. Bull. 84 (10), 3137–3180.

Djamour, Y., Vernant, P., Nankali, H.R., Tavakoli, F., 2011. NW Iran-eastern Turkey present-day kinematics: results from the Iranian permanent GPS network. Earth Planet. Sci. Lett. 307 (1–2), 27–34.

Fialko, Y., 2006. Interseismic strain accumulation and the earthquake potential on the southern San Andreas fault system. Nature 441, 968–971.

Gabrielov, A.M., Levshina, T.A., Rotwain, I.M., 1990. Block model of earthquake sequence. Phys. Earth Planet. Inter. 61, 18–28.

Hacker, B.R., Yin, A., Christie, J.M., Davis, G.A., 1992. Stress magnitude, strain rate, and rheology of extended Middle Continental Crust inferred from quartz grain sizes in the Whipple Mountains, California. Tectonics 11, 36–46.

Hudson, J.A., 2000. The effect of fluid pressure on wave speeds in a cracked solid. Geophys. J. Int. 143, 302–310.

Iio, Y., 1997. Frictional coefficient on faults in a seismogenic region inferred from earthquake mechanism solutions. J. Geophys. Res. 102, 5403–5412.

Ismail-Zadeh, A., Tackley, P., 2010. Computational Methods for Geodynamics. Cambridge University Press, Cambridge, pp. 313.

Ismail-Zadeh, A.T., Keilis-Borok, V.I., Soloviev, A.A., 1999. Numerical modelling of earthquake flows in the southeastern Carpathians (Vrancea): effect of a sinking slab. Phys. Earth Planet. Inter. 111, 267–274.

Ismail-Zadeh, A.T., Le Mouël, J.-L., Soloviev, A., Tapponnier, P., Vorobieva, I., 2007. Numerical modelling of crustal block-and-fault dynamics, earthquakes and slip rates in the Tibet-Himalayan region. Earth Planet. Sci. Lett. 258, 465–485.

Ismail-Zadeh, A., Soloviev, A., Sokolov, V., Vorobieva, I., Muller, B., Schilling, F., 2018. Quantitative modeling of the lithosphere dynamics, earthquakes and seismic hazard. Tectonophysics 746, 624–647.

Jackson, J., 1992. Partitioning of strike-slip and convergent motion between Eurasia and Arabia in eastern Turkey. J. Geophys. Res. 97, 12471–12479.

Jackson, J., Priestley, K., Allen, M., Berberian, M., 2002. Active tectonics of the South Caspian Basin. Geophys. J. Int. 148 (2), 214–245.

Kadirov, F.A., Floyd, M., Reilinger, R., Alizadeh, A.A., Guliyev, I.S., Mammadov, S.G., Safarov, R.T., 2015. Active geodynamics of the Caucasus region: implication for earthquake hazards in Azerbaijan. Proc. Azerbaijan Academy of Sciences, Earth. Sciences 3, 3–17.

Karakhanian, A.S., Trifonov, V.G., Philip, H., Avagyan, A., Hessami, K., Jamali, F., Bayraktutan, M.S., Bagdassarian, H., Arakelian, S., Davtian, V., Adilkhanyan, A., 2004. Active faulting and natural hazards in Armenia, eastern Turkey and northwestern Iran. Tectonophysics 380, 189–219.

Karakhanian, A., Vernant, P., Doerflinger, E., Avagyan, A., Philip, H., Aslanyan, R., Champollion, C., Arakelyan, S., Collard, P., Baghdasaryan, H., Peyret, M., Davtyan, V., Calais, E., Masson, F., 2013. GPS constraints on continental deformation in the Armenian region and Lesser Caucasus. Tectonophysics 592, 39–45.

Keilis-Borok, V.I., 1990. The lithosphere of the Earth as non-linear system with implications for earthquake prediction. Rev. Geophys. 28, 19–34.

Keilis-Borok, V., Ismail-Zadeh, A., Kossobokov, V., Shebalin, P., 2001. Non-linear dynamics of the lithosphere and intermediate-term earthquake prediction. Tectonophysics 338, 247–259.

Khain, V.Y., 1975. Structure and main stages in the tectono-magmatic development of the Caucasus: an attempt at geodynamic interpretation. Am. J. Sci. A 275, 131–156.

Kondorskaya, N.V., Shebalin, N.V., 1977. New Catalog of Strong Earthquakes in the U.S.S.R. From Ancient Times Through 1975. (Moscow, Nauka, 536 pp. (translated into English by the World Data Center A for Solid Earth Geophysics in 1982)).

Mosar, J., Kangarli, T., Bochud, M., et al., 2010. Cenozoic-recent tectonics and uplift in the Greater Caucasus: a perspective from Azerbaijan. In: Sosson, M., Kaymakci, N., Stephenson, R., Bergerat, F., Starostenko, V. (Eds.), Sedimentary Basin Tectonics from the Black Sea and Caucasus to the Arabian Platform. vol. 3. pp. 261–280 London: Special Publications, Geological Society; 2010.

Mumladze, T., Forte, A.M., Cowgill, E.S., Trexler, C.C., Niemi, N.A., Yıkılmaz, M.B., Kellogg, L.H., 2015. Subducted, detached, and torn slabs beneath the Greater Caucasus. GeoResJ 5, 36–46.

Nikonov, A., Nikonova, K., 1986. The strongest earthquake in the Transcaucasus, September 30, 1139. Voprosy Ingenernoy Seismologii 27, 152–183 (in Russian).

Panahi, B.M., 2006. Seismicity in Azerbaijan and adjacent Caspian Sea. In: Ismail-Zadeh, A. (Ed.), Recent Geodynamics, Georisk and Sustainable Development in the Black Sea to Caspian Sea Region, AIP Conference Proceedings. 825. pp. 3–10.

Peresan, A., Vorobieva, I., Soloviev, A., Panza, G., 2007. Simulation of seismicity in the block-structure model of Italy and its surroundings. Pure Appl. Geophys. 164, 2193–2234.

Philip, H., Avagyan, A., Karakhanian, A., Ritz, J.-F., Rebai, S., 2001. Estimating slip rates and recurrence intervals for strong earthquakes along an intracontinental fault: example of the Pambak–Sevan–Sunik fault (Armenia). Tectonophysics 343 (3–4), 205–232.

Reasenberg, P.A., Simpson, R.W., 1992. Response of regional seismicity to the static stress change produced by the Loma Prieta Earthquake. Science 255, 1687–1690.

Reilinger, R.E., McClusky, S., Vernant, P., Lawrence, S., Ergintav, S., Cakmak, R., Ozener, H., Kadirov, F., Guliev, I., Stepanyan, R., Nadariya, M., Hahubia, G., Mahmoud, S., Sakr, K., Arrajehi, A., Paradissis, D., Al-Aydrus, A., Prilepin, M., Guseva, T., Evren, E., Dmitrotsa, A., Filikov, S.V., Gomez, F., Al-Ghazzi, R., Karam, G., 2006. GPS constraints on continental deformation in the Africa-Arabia-Eurasia continental collision zone and implications for the dynamics of plate interactions. J. Geophys. Res. BO5411. https://doi.org/10.1029/2005JB 004051.

Rice, J.R., 2006. Heating and weakening of faults during earthquake slip. J. Geophys. Res. 111, B05311. https://doi.org/10.1029/2005JB004006.

Ritz, J.-F., Avagyan, A., Mkrtchyan, M., Nazaric, H., Blard, P.-H., Karakhanian, A., Philip, H., Balescu, S., Mahan, S., Huot, S., Münch, P., Lamothe, M., 2016. Active tectonics within the NW and SE extensions of the Pambak-Sevan-Syunik fault: implications for the present geodynamics of Armenia. Quat. Int. 395, 61–78.

Saintot, A., Angelier, J., 2002. Tectonic paleostress fields and structural evolution of the NW-Caucasus fold-and-thrust belt from Late Cretaceous to Quaternary. Tectonophysics 357, 1–31. https://doi.org/10.1016/s0040-1951(02)00360-8.

Şengör, A.M.C., Kidd, W.S.F., 1979. Post-collisional tectonics of the Turkish-Iranian plateau and a comparison with Tibet. Tectonophysics 55, 361–376.

Sokolov, V., Ismail-Zadeh, A., 2015. Seismic hazard from instrumentally recorded, historical and simulated earthquakes: application to the Tibet-Himalayan region. Tectonophysics 657, 187–204.

Sokolov, V., Ismail-Zadeh, A., 2016. On the use of multiple-site estimations in probabilistic seismic hazard assessment. Bull. Seismol. Soc. Am. 106 (5), 2233–2243.

Soloviev, A.A., Gorshkov, A.I., 2017. Modeling the dynamics of the block structure and seismicity of the Caucasus. Izv., Phys. Solid Earth 53 (3), 321–331.

Soloviev, A., Ismail-Zadeh, A., 2003. Models of dynamics of block-and-fault systems. In: Keilis-Borok, V.I., Soloviev, A.A. (Eds.), Nonlinear Dynamics of the Lithosphere and Earthquake Prediction. Springer, Heidelberg, pp. 71–138.

Tan, O., Taymaz, T., 2006. Active tectonics of the Caucasus: earthquake source mechanisms and rupture histories obtained from inversion of teleseismic body waveforms. In: Dilek, Y., Pavlides, S. (Eds.), Postcollisional Tectonics and Magmatism in the Mediterranean Region and Asia. Geological Society of America Special Paper 409. pp. 531–578.

Tod, S.R., 2002. The effects of stress and fluid pressure on the anisotropy of interconnected cracks. Geophys. J. Int. 149, 149–156.

Trifonov, V.G., Karakhanian, A.S., Kozhurin, A.J., 1994. Active faults of the collision area between the Arabian and the Eurasian plates. In: Proc. of the Conference on Continental Collision Zone Earthquakes and Seismic Hazard Reduction, Yerevan, pp. 56–79.

Tskhakaia, A., 1950. Essay on the Development of Seismology in Georgia. Georgian Academy of Sciences, Tbilisi (in Russian).

Turcotte, D.L., 1999. Seismicity and self-organized criticality. Phys. Earth Planet. Inter. 111, 275–294.

Turcotte, D.L., Schubert, G., 2002. Geodynamics, 2nd ed. Cambridge University Press, Cambridge (456 pp.).

Ulomov, V.I., Medvedeva, N.S. (Eds.), 2014. Dedicated Catalog of Earthquake of the Norther Eurasia. O.Y. Smidt Institute of Physics of the Earth, Russian Academy of Sciences. http://seismos-u.ifz.ru/documents/Eartquake-Catalog-%D0%A1%D0%9A%D0%97.pdf.

Veber, V., 1904. Recherches preliminaries sur le tremblement de terre a Chemakha. In: Academie Imperiale des Sciences, Comptes Rendus des Seances de La Commission Sismique Permanente. Tome I. St.-Petersbourg. Russie, pp. 238–240.

Vernant, P., Chery, J., 2006. Low fault friction in Iran implies localized deformation for the Arabia–Eurasia collision zone. Earth Planet. Sci. Lett. 246, 197–206.

Vorobieva, I., Mandal, P., Gorshkov, A., 2017. Block-and-fault dynamics modelling of the Himalayan frontal arc: implications for seismic cycle, slip deficit, and great earthquakes. J. Asian Earth Sci. 148, 131–141.

Wells, D.L., Coppersmith, K.J., 1994. New empirical relationships among magnitude, rupture length, rupture width, rupture area, and surface displacement. Bull. Seismol. Soc. Am. 84, 974–1002.

Zonenshain, L.P., Le Pichon, X., 1986. Deep basins of the Black Sea and Caspian Sea as remnants of Mesozoic back-arc basins. Tectonophysics 123, 181–211.